SHARP BOUNDARY ELECTROCARDIAC SIMULATIONS[*]

SHUAI XUE[†], HYUNKYUNG LIM[†], JAMES GLIMM[‡], FLAVIO H. FENTON[‡], AND ELIZABETH M. CHERRY[§]

Abstract. We present a sharp boundary electrocardiac simulation model based on the finite volume embedded boundary method for the solution of voltage dynamics in irregular domains with anisotropy and a high degree of anatomical detail. This method is second order accurate uniformly up to boundaries and is able to resolve small features without the use of fine meshes. This capability is necessary to enable the repeated simulations required for future verification and validation and uncertainty quantification studies of defibrillation, where fine-scale heterogeneities, such as those formed by small blood vessels, play an important role and require resolution.

Key words. embedded boundary method, cardiac electrophysiology, tensor diffusion

AMS subject classifications. 65M08, 65M12, 65N08, 65N12

DOI. 10.1137/15M1019283

1. Introduction. Heart failure is a leading cause of death in the industrial world [29, 11], with a large effort devoted to understanding the normal and abnormal behaviors of the heart [14]. Here we model the electrical activity within the cardiac cells, which govern their contractions and force the flow of blood. We address the numerical analysis aspect of a planned verification and validation (V&V) and uncertainty quantification (UQ) study for design of defibrillation surgical implants. The key issue is to resolve electrical signals near fine-scale tissue details without excessive grid requirements, as V&V/UQ studies depend on numerous repeated simulations.

The governing equation consists of a diffusion equation and a reaction source term depending on ionic currents. The main result of this paper is the introduction of a sharp boundary treatment of the voltage diffusion equation into cardiac models. The resulting algorithm allows arbitrary order of accuracy in the L_∞ norm and as implemented here with algorithm details included is second order accurate. Local mesh refinement techniques, such as h-refinement [39] and p-refinement [58], can be adopted to improve the numerical resolution on coarse grids. Both the arbitrary order of accuracy and the second order details are new for the case of tensor diffusion, as considered here. The code is based on the finite volume discretization of the voltage equation, based on the embedded boundary method (EBM). We solve the bidomain equations, representing the cardiac tissue as overlapping intracellular and extracellular domains [14], as is needed in defibrillation modeling. For this same purpose we emphasize the resolution of small discontinuities, such as blood vessels and

[†]Department of Applied Math and Statistics, Stony Brook University, Stony Brook, NY 11794 (xueshuai87@gmail.com, hyulim@ams.sunysb.edu, glimm@ams.sunysb.edu).

[‡]School of Physics, Georgia Institute of Technology, Atlanta, GA 30332 (flavio.fenton@physics.gatech.edu).

[§]School of Mathematical Sciences, Rochester Institute of Technology, Rochester, NY 14623 (excsma@rit.edu).

infarct scars, which produce virtual electrodes when defibrillation voltage is applied [63, 40], in addition to the complex dynamics due to irregular boundaries [49, 10].

The major motivation of this work is a planned V&V and UQ study of defibrillating voltages applied at electrodes on the exterior of the heart as outlined by Pathmanathan et al. in [45]. The purpose of the defibrillating voltage is to reset the electrical state of the heart, so that normal heartbeat cycles will follow. Such V&V/UQ studies require repeated simulations, and their success depends in part on the number feasible within a given resource limit. Thus the ability to obtain useful solutions on a coarse mesh is the primary figure of merit considered here, which is achieved by applying the high order numerical method introduced in this paper.

A number of models of the ionic currents have been proposed at differing levels of completeness and complexity [22, 38]. The canine ventricular cell model of Flaim, Giles, and McCulloch [28] includes as many as 87 variables, the Bondarenko, Bett, and Rasmusson model [5] involves more that 100 variables. Although these complex models reproduce existing experimental results through careful selection of parameters, high parameter numbers often affect model robustness and introduce inconsistencies between models of the same animal species and specific regions of the heart [9], not to mention their computational expenses. Several reduced models have been proposed [42, 19, 24, 42, 34]. The Fenton–Karma (FK) three-variable model is widely used, due to its capability to maintain most of the quantitative properties of the more complicated models, while reducing the computational complexity significantly [22]. These properties have made the FK model popular in a wide range of studies, including vortex dynamics in the myocardium [24], mechanisms for discordant alternans [62], temperature effects [25, 27], and the promising field of low-energy defibrillation [8, 26].

The paper is organized as follows. The governing electrocardiac equations are presented in section 2. In section 3 we explain the numerical method. The treatment of the EBM follows ideas of [41, 61]. We present what appears to be a new feature for this method, the solution with anisotropic diffusion. Our solution is shown to be second order accurate in the L_∞ (as well as the L_1) norm. Use of the L_∞ norm for convergence analysis means that the order of accuracy is maintained uniformly up to the boundary. Section 4 is devoted to the verification of our method through code comparison to the previously verified and validated phase field (PF) method [22]. In section 5, we illustrate the resolution of the method by showing the flow of electrical signals around small blood vessels, and for the bidomain model, the enhanced coupling between the two voltage systems that results. As mentioned earlier, blood vessels of a certain size play an important role in the defibrillation process [40, 4]. In a separate study, the smallest relevant blood vessels have a diameter set by the blood vessel wall resistivity and have been estimated as 200 μm [4]. From this fact and the present work (see especially the key Figure 5), we require about four cells across the blood vessel. Thus we see that the maximum useful mesh size is about $200/4 = 50$ μm. Compared to the heart itself, with a diameter of 8 cm [47], we see the importance of mesh resolution considerations. Finally, section 6 contains our conclusions and a discussion of some promising improvements and extensions.

2. Governing equations. The evolution of voltages in cardiac tissue is described by a system of reaction-diffusion equations, with the transmembrane ionic currents defining the reaction and the electric potential equations solved as a diffusion process. Both the currents and the potentials represent averages over a region containing many cells. The problem is complicated by
- complex, stiff, and interacting reaction rates;

- thin walls of the quasi-two-dimensional heart chamber with small-scale features such as blood vessels or isolated regions of diseased tissue; and
- strongly anisotropic diffusion, with more rapid diffusion along directions parallel to the fibers than directions perpendicular to the fibers.

Since its introduction in the late 1970s [59], the bidomain model has been adopted widely in cardiovascular studies, such as induction of reentry and fibrillation [3, 16, 50], the effects of virtual electrodes on defibrillation [20, 33, 51], and the cardiac tissue responses to defibrillation shocks [21, 1, 2]. In this model, the unequal anisotropy ratios of the intracellular and extracellular spaces are expressed explicitly, which better reflects the fact, compared with the simplistic monodomain model, that myocytes are embedded in a complex network of body fluid and fine capillaries, etc. As the defibrillating voltage is deposited in the extracellular tissue, but its beneficial effect occurs within the cellular tissue, the bidomain model, which couples the two, is needed for defibrillation studies.

We use Ω to denote the solution domain, which consists of $\mathbb{H}$, the heart tissue, and $\mathbb{T} = \Omega \backslash \mathbb{H}$, the perfusing bath (including interior cavities and blood vessels). The bidomain equations and boundary conditions are

$$\nabla \cdot (D_i \nabla \phi) + \nabla \cdot (D_i \nabla \phi_e) = \chi \left(C_m \frac{\partial \phi}{\partial t} + I_{\text{ion}}(\phi, \mathbf{y}) \right), \quad \mathbf{x} \in \mathbb{H}, \tag{2.1}$$

$$\nabla \cdot (D_i \nabla \phi) + \nabla \cdot ((D_i + D_e) \nabla \phi_e) = 0, \quad \mathbf{x} \in \mathbb{H}, \tag{2.2}$$

$$\frac{\partial \mathbf{y}}{\partial t} = g(\phi, \mathbf{y}), \quad \mathbf{x} \in \mathbb{H}, \tag{2.3}$$

$$\nabla \cdot (D_t \nabla \phi_t) = 0, \quad \mathbf{x} \in \mathbb{T}, \tag{2.4}$$

$$\phi_e - \phi_t = 0, \quad \mathbf{x} \in \partial \mathbb{H}, \tag{2.5}$$

$$D_e \nabla \phi_e \cdot \mathbf{n} - D_t \nabla \phi_t \cdot \mathbf{n} = 0, \quad \mathbf{x} \in \partial \mathbb{H}, \tag{2.6}$$

$$D_i \nabla \phi \cdot \mathbf{n} + D_i \nabla \phi_e \cdot \mathbf{n} = 0, \quad \mathbf{x} \in \partial \mathbb{H}, \tag{2.7}$$

$$D_t \nabla \phi_t \cdot \mathbf{n} = 0, \quad \mathbf{x} \in \partial \mathbb{T} \backslash \partial \mathbb{H}, \tag{2.8}$$

where $\phi = \phi_i - \phi_e$ is the transmembrane voltage, which is the difference between the intracellular potential ϕ_i and extracellular potential ϕ_e; ϕ_t is the electric potential in $\mathbb{T}$; D_i, D_e, and D_t are the anisotropic conductivity tensors in the intracellular, extracellular, and perfusing bath regions, respectively; C_m is the membrane capacitance and χ is the surface to volume ratio; and I_{ion} denotes the ionic current term, which is controlled by a gate function g. We adopt the parameter values in [53] to perform numerical simulations in the following sections.

The elements of D_i and D_e are determined by the local myocardial fiber orientation [23],

$$D_* = \beta_*^{\perp} \mathbf{I} + \left(\beta_*^{\|} - \beta_*^{\perp} \right) \mathbf{f} \mathbf{f}^T, \tag{2.9}$$

where $\beta_*^{\|}$ and $\beta_*^{\perp}$ (*=i, e), are the conductivities longitudinal and transversal to the fiber, which is parallel to a unit vector $\mathbf{f}$. As in [53], we assume D_t to be an isotropic tensor,

$$D_t = \beta_t \mathbf{I}, \tag{2.10}$$

where β_t is the scalar conductivity in $\mathbb{T}$.

The determination of the elements of D_t follows a similar manner and depends on the physiological properties of the perfusing bath.

We follow the FK [24] three-variable model, which achieves a satisfactory balance between accuracy and simplicity. In the FK model

$$(2.11) \qquad I_{\mathrm{ion}}\left(\phi,\mathbf{y}\right)=I_{\mathrm{fi}}\left(\phi,v\right)+I_{\mathrm{so}}\left(\phi\right)+I_{\mathrm{si}}\left(\phi,w\right),$$

where I_{fi}, I_{so}, and I_{si} denote the fast-inward, slow-outward, and slow-inward ionic currents, respectively, and $\mathbf{y}=(v,w)$ is the vector of gate variables controlling the fast- and slow-inward components. A detailed discussion of the FK model can be found in [24].

For the boundary conditions, we assume $\mathbb{T}$ to be electrically isolated from the environment, which leads to the no-flux condition (2.8). As in [35], we assume there is a direct connection between $\mathbb{T}$ and the extracellular domain, while the intracellular domain is completely isolated from $\mathbb{T}$, as shown in (2.5)–(2.7).

3. Numerical methods.

3.1. Overview of numerical methods. The goal of the present work is to resolve small features within the diffusion equation on computationally feasible grids. At issue is the number of grid cells needed to obtain convergence relative to the fine-scale feature size. Additionally, the sharp boundaries (of the heart tissue or of the feature) are a numerical issue, so that localized convergence near the heart boundary or near a feature is an important issue.

We mention commonly used methods for the solution of the diffusion equation, but a full comparison of these methods is beyond the scope of the present paper.

Ghost cell [13, 44]. The ghost cell method is very simple. Missing data points near a domain boundary for a finite difference stencil used to solve the diffusion equation are added by extrapolation from interior points along coordinate directions, even ambiguously if needed in higher dimensions near concave boundary segments. In effect, this plan is equivalent (or nearly so) to a stair-step interface, located at the cell edges that mark a transition from a cell center which lies in the domain to a cell center outside of the domain. The original reference is first order [18], but extensions to second order accuracy have been given [30].

Phase field [23, 6]. An additional equation (the PF equation) interpolates between the inside and the outside, with a typical width of five cells. This method is first order accurate. In [7] the PF width is reduced to zero in a mathematical limit, leading to a thin or thinner interface transition region. The method appears to be first order accurate (when a sharp interface is specified as input), but the order of convergence has not been documented.

Immersed boundary method [46, 43]. The Heaviside function associated with the boundary is replaced with a numerically spread Heaviside function, The interface width is several cells wide, with the width depending on the size of the jump in the coefficients. The method and its accuracy are well documented. It is first order accurate.

Finite elements [48, 12, 57]. The method requires a body-fitting grid adapted to complex problem features.

Immersed interface method (IIM) [37]. Here there is a serious attempt to treat the cut cells coherently, with additional degrees of freedom added within the cut cells to describe the solution there.

Embedded boundary method [41, 61]. This method is similar to IIM but differs in detail. It is a well-documented method and will be discussed in section 3.2. It has second order convergence in L_∞ (uniformly up to the boundary), so that boundary region anomalies will not occur in the solution.

3.2. Embedded boundary method. On the basis of the above survey, the EBM (and possibly also IIM) appears to be the most suitable for high resolution of fine-detailed features in the heart geometry, with blood vessels and/or diseased tissues defining the fine-scale structures.

We use the EBM to discretize the parabolic subsystem of the FK model. Originally proposed by Colella and others [32, 41, 54], the EBM method maintains sharp boundaries and interfaces in geometrically complex domains [52, 61]. It is locally conservative and robust in marginally resolved calculations [54]. The EBM has recently been extended to solve the elliptic interface problem [17, 52, 61] and the two-phase incompressible flow problem [60].

EBM is a finite difference method, which treats cut cells (grid cells partly inside the cardiac tissue and partly outside) in a manner differently from the regular, noncut cells. The computational domain is thus discretized as a collection of control volumes formed by the intersection of the domain with rectangular Cartesian grid cells. Whether a cell center is inside or outside the domain, the corresponding primary unknowns are always cell-centered.

To achieve accurate solutions of the voltage equation, additional degrees of freedom are needed for the cut cells. It is necessary to capture the crossings of the cardiac anatomy with the underlying Cartesian grids to apply the EBM. This geometrical information is readily available in most state-of-art mesh generation tools and we adopt the FronTier library [31]. The diffusion process in a cut cell has zero values in the outside portion of the cut cell and "normal" values in the interior portion of the cut cell. Thus the tensor diffusivities defined in the interior region must be supplemented by information on the size of the interior and exterior portions of the cut cell. With tensor, as opposed to scalar, diffusivities, derivatives of the voltage in x-, y-, and z-directions, instead of only the derivative normal to the tissue boundary, are involved in the calculation of boundary flux.

The result, as analyzed in [41], is a second order accurate method in the L_∞ norm, meaning that anomalous boundary signals will not occur in the method. This result is established for scalar diffusion coefficients only, and the cited reference explains the method in this case only. Accordingly, we detail here the discretization and the modifications needed for tensor diffusion coefficients, and we document in section 4 convergence rates for this case, a new contribution of the present paper. The algorithm is organized in a manner that allows formulation for an arbitrary order of accuracy.

To solve the nonlinear system of equations in the bidomain model numerically, we adopt the operator-splitting scheme proposed by Dos Santos et al. [53]. In this discretization, each time step consists of the solution of three subproblems, i.e., a parabolic PDE, a system of nonlinear ODEs, and a system of elliptic PDEs. The second order Crank–Nicolson method and first order forward-Euler method are used to solve the parabolic PDE and the system of nonlinear ODEs, respectively, which leads to the following semidiscrete system:

$$(3.1) \quad 1. \quad \left(1 - \frac{\Delta t}{2}L_i\right)\varphi^{n+1/2} = \left(1 + \frac{\Delta t}{2}L_i\right)\varphi^n + \Delta t\, L_i\, \varphi_e^n,$$

$$(3.2) \quad 2. \quad \varphi^{n+1} = \varphi^{n+1/2} - \Delta t\, I_{\text{ion}}\left(\varphi^{n+1/2}, y^n\right)/\left(\chi C_m\right),$$

$$(3.3) \quad y^{n+1} = y^n + \Delta t\, g\left(\varphi^{n+1/2}, y^n\right),$$

$$(3.4) \quad 3. \quad (L_i + L_e)\,\varphi_e^{n+1} = -L_i\,\varphi^{n+1},$$

$$(3.5) \quad L_t\,\varphi_t^{n+1} = 0,$$

where L_i, L_e, and L_t denote the operators $\nabla \cdot (D_i \nabla) / (\chi C_m)$, $\nabla \cdot (D_e \nabla) / (\chi C_m)$, and $\nabla \cdot (D_t \nabla)$; φ^{n+1}, φ_e^{n+1}, φ_t^{n+1}, and y^n are discretizations of ϕ, ϕ_e, ϕ_t, and y at time step n. The von Neumann analysis similar to that in [32] shows the above scheme is unconditionally stable.

The EBM method is applied to solve the parabolic PDE (3.1) and the system of elliptic PDEs (3.4), (3.5) in the above semidiscrete system. To give a clear explanation of the EBM method, it is necessary to make a mathematically unambiguous description of the spatial discretization of the solution domain. We will follow the notation given by Schwartz et al. [54], describing the discretization of a general irregular domain Ω embedded in a Cartesian grid. In the merit of simpler notation, we assume the Cartesian grid is equidistant in all axial directions, although the following numerical algorithm remains valid in the general case of variant mesh spacings. The Cartesian grid consists of rectangular cuboids $\Gamma_{\boldsymbol{i}} = \left[\left(\boldsymbol{i} - \frac{1}{2} \boldsymbol{u} \right) h, \left(\boldsymbol{i} + \frac{1}{2} \boldsymbol{u} \right) h \right]$, $\boldsymbol{i} \in \mathbb{Z}^3$, where $\boldsymbol{u}$ is the vector with all entries equal to one, and h is the mesh spacing. We define control volumes $V_{\boldsymbol{i}} = \Gamma_{\boldsymbol{i}} \cap \Omega$ and face elements $A_{\boldsymbol{i} \pm \frac{1}{2} \boldsymbol{e}_s}$, which are the intersections of $\partial V_{\boldsymbol{i}}$ with the coordinate planes $\left\{ \boldsymbol{x} : x_s = \left(i_s \pm \frac{1}{2} \right) h \right\}$. Here $\boldsymbol{e}_s$ is the unit vector in the s-direction. Similarly we define the boundary elements $A_{\boldsymbol{i}}^B$ to be $\partial \Omega \cap \Gamma_{\boldsymbol{i}}$. Then we have the following decomposition of the surfaces of control volumes:

$$\partial V_{\boldsymbol{i}} = \left(\bigcup_{s=1}^d A_{\boldsymbol{i} \pm \frac{1}{2} \boldsymbol{e}_s} \right) \bigcup A_{\boldsymbol{i}}^B .$$

With the above definitions of the basic geometric objects, several real-valued quantities necessary for the EBM discretization can be introduced.

- Dimensionless area: volume fractions $\kappa_{\boldsymbol{i}} = |V_{\boldsymbol{i}}| h^{-d}$, face apertures $\alpha_{\boldsymbol{i} \pm \frac{1}{2} \boldsymbol{e}_s} = |A_{\boldsymbol{i} \pm \frac{1}{2} \boldsymbol{e}_s}| h^{-(d-1)}$, and boundary apertures $\alpha_{\boldsymbol{i}}^B = |A_{\boldsymbol{i}}^B| h^{-(d-1)}$.
- Centroids and average outward normals to the boundary

$$\tag{3.6} \boldsymbol{x}_{\boldsymbol{i}} = \frac{1}{|V_{\boldsymbol{i}}|} \int_{V_{\boldsymbol{i}}} \boldsymbol{x} \, dV,$$

$$\tag{3.7} \boldsymbol{x}_{\boldsymbol{i} \pm \frac{1}{2} \boldsymbol{e}_s} = \frac{1}{\left| A_{\boldsymbol{i} \pm \frac{1}{2} \boldsymbol{e}_s} \right|} \int_{A_{\boldsymbol{i} \pm \frac{1}{2} \boldsymbol{e}_s}} \boldsymbol{x} \, dA,$$

$$\tag{3.8} \boldsymbol{x}_{\boldsymbol{i}}^B = \frac{1}{|A_{\boldsymbol{i}}^B|} \int_{A_{\boldsymbol{i}}^B} \boldsymbol{x} \, dA,$$

$$\tag{3.9} \boldsymbol{n}_{\boldsymbol{i}}^B = \frac{1}{|A_{\boldsymbol{i}}^B|} \int_{A_{\boldsymbol{i}}^B} \boldsymbol{n} \, dA,$$

where $\boldsymbol{n}^B$ is the outward normal to $\partial \Omega$.

Since the EBM method discussed here can be used to solve a variety of elliptic and parabolic PDEs, we will illustrate the detailed scheme in a more general way than the specific application for the bidomain model. The main innovation of the new scheme is in the discretization of the flux through surfaces of each control volume. We apply the EBM method to the Poisson equation with the Dirichlet boundary condition

$$\tag{3.10} \nabla \cdot D \nabla \psi = \rho(\boldsymbol{x}) \ in \, \Omega,$$

$$\tag{3.11} \psi = g_d(\boldsymbol{x}) \ on \, \partial \Omega,$$

where D is an anisotropic diffusion tensor and ρ and g_d are given functions. Brief discussions indicating the construction of high order schemes to parabolic equations and Neumann boundary conditions will be given later.

In the EBM method, we average (3.10) over each control volume $\Gamma_{\boldsymbol{i}}$ and use the divergence theorem to transform the volume integrals into integrals over the boundary $\partial \Gamma_{\boldsymbol{i}}$,

$$(3.12) \qquad \int_{V_{\boldsymbol{i}}} \rho \, dV = \sum_{\pm=+,-} \sum_{s=1}^{d} \int_{A_{\boldsymbol{i}\pm\frac{1}{2}\boldsymbol{e}_s}} \vec{F} \cdot \boldsymbol{n} \, dA + \int_{A_{\boldsymbol{i}}^B} \vec{F} \cdot \boldsymbol{n} \, dA,$$

where the flux term $\vec{F} = D\nabla\psi$. As in [15], we define the notation $\langle \cdot \rangle_{\mathbb{S}}$ as the average of a quantity over the domain $\mathbb{S}$ (two-dimensional (2D) or 3D). Then (3.12) can be rewritten as

$$(3.13) \qquad \langle \rho \rangle_{\boldsymbol{i}} = \frac{1}{\kappa_{\boldsymbol{i}} h} \left(\sum_{\pm} \sum_{s} \alpha_{\boldsymbol{i}\pm\frac{1}{2}\boldsymbol{e}_s} \left\langle \vec{F} \cdot \boldsymbol{n} \right\rangle_{\boldsymbol{i}\pm\frac{1}{2}\boldsymbol{e}_s} + \alpha_{\boldsymbol{i}}^B \left\langle \vec{F} \cdot \boldsymbol{n} \right\rangle_{i,B} \right),$$

where the further notation simplifications $\langle \cdot \rangle_{\boldsymbol{i}} = \langle \cdot \rangle_{V_{\boldsymbol{i}}}$, $\langle \cdot \rangle_{\boldsymbol{i}\pm\frac{1}{2}\boldsymbol{e}_s} = \langle \cdot \rangle_{A_{\boldsymbol{i}\pm\frac{1}{2}\boldsymbol{e}_s}}$, and $\langle \cdot \rangle_{i,B} = \langle \cdot \rangle_{A_{\boldsymbol{i}}^B}$ are introduced. A variety of high order schemes can be introduced by applying appropriate quadrature rules to the calculation of average values in (3.13). At first glance, an nth order quadrature rule over $V_{\boldsymbol{i}}$ and $(n+1)$th order quadrature rules over $A_{\boldsymbol{i}\pm\frac{1}{2}\boldsymbol{e}_s}$ and $A_{\boldsymbol{i}}^B$ are necessary for the construction of nth order accurate finite volume schemes for (3.13). However, a modified equation analysis as in [32] shows that approximating $\langle \vec{F} \cdot \boldsymbol{n} \rangle_{\boldsymbol{i}\pm\frac{1}{2}\boldsymbol{e}_s}$ and $\langle \vec{F} \cdot \boldsymbol{n} \rangle_{i,B}$ to the nth order of accuracy is sufficient to make the solution errors nth order convergent. For high order quadrature rules on irregular domains the reader can refer to [36, 64].

In the remaining part of the paper, we will focus on a second order discretization of (3.13), which requires us to approximate both $\langle \vec{F} \cdot \boldsymbol{n} \rangle_{\boldsymbol{i}\pm\frac{1}{2}\boldsymbol{e}_s}$ and $\langle \vec{F} \cdot \boldsymbol{n} \rangle_{i,B}$ to second order accuracy. It is easy to verify that

$$(3.14) \qquad \left\langle \vec{F} \cdot \boldsymbol{n} \right\rangle_{\boldsymbol{i}\pm\frac{1}{2}\boldsymbol{e}_s} = D\left(\boldsymbol{x}_{\boldsymbol{i}\pm\frac{1}{2}\boldsymbol{e}_s}\right) \nabla\psi\left(\boldsymbol{x}_{\boldsymbol{i}\pm\frac{1}{2}\boldsymbol{e}_s}\right) \cdot \boldsymbol{e}_s + O\left(h^2\right),$$

$$(3.15) \qquad \left\langle \vec{F} \cdot \boldsymbol{n} \right\rangle_{i,B} = D\left(\boldsymbol{x}_{\boldsymbol{i}}^B\right) \nabla\psi\left(\boldsymbol{x}_{\boldsymbol{i}}^B\right) \cdot \boldsymbol{n}_{\boldsymbol{i}}^B + O\left(h^2\right).$$

Since we assume the geometric quantities $\boldsymbol{x}_{\boldsymbol{i}\pm\frac{1}{2}\boldsymbol{e}_s}$, $\boldsymbol{x}_{\boldsymbol{i}}^B$, and $\boldsymbol{n}_{\boldsymbol{i}}^B$ are accurate to $O\left(h^2\right)$, second order approximations to the gradient $\nabla\psi$ at the centroids $\boldsymbol{x}_{\boldsymbol{i}\pm\frac{1}{2}\boldsymbol{e}_s}$ and $\boldsymbol{x}_{\boldsymbol{i}}^B$ suffices to make the whole scheme $O\left(h^2\right)$ accurate.

3.3. The gradient approximation at a face centroid. We define the discrete variable ϕ, $\phi_{\boldsymbol{i}} \approx \psi\left(\left(\boldsymbol{i} + \frac{1}{2}\boldsymbol{u}\right)h\right)$. Then the gradient at the face centroids $\nabla\psi(\boldsymbol{x}_{\boldsymbol{i}\pm\frac{1}{2}\boldsymbol{e}_s})$ can be approximated by linear combinations of $\phi_{\boldsymbol{i}}$ and the boundary values. At any given face $A_{\boldsymbol{i}\pm\frac{1}{2}\boldsymbol{e}_s}$, two types of approximations of ψ's partial derivatives need to be constructed: $\phi'_{\boldsymbol{i}\pm\frac{1}{2}\boldsymbol{e}_s} \approx \frac{d\psi}{de_s}(\boldsymbol{x}_{\boldsymbol{i}\pm\frac{1}{2}\boldsymbol{e}_s})$, the derivative along the axis normal to the face; and $\phi'_{\boldsymbol{i}\pm\frac{1}{2}\boldsymbol{e}_{s'}} \approx \frac{d\psi}{de_{s'}}(\boldsymbol{x}_{\boldsymbol{i}\pm\frac{1}{2}\boldsymbol{e}_{s'}})$, $s' \neq s$, the derivatives along axes parallel to the face. We detail the numerical schemes used in each case.
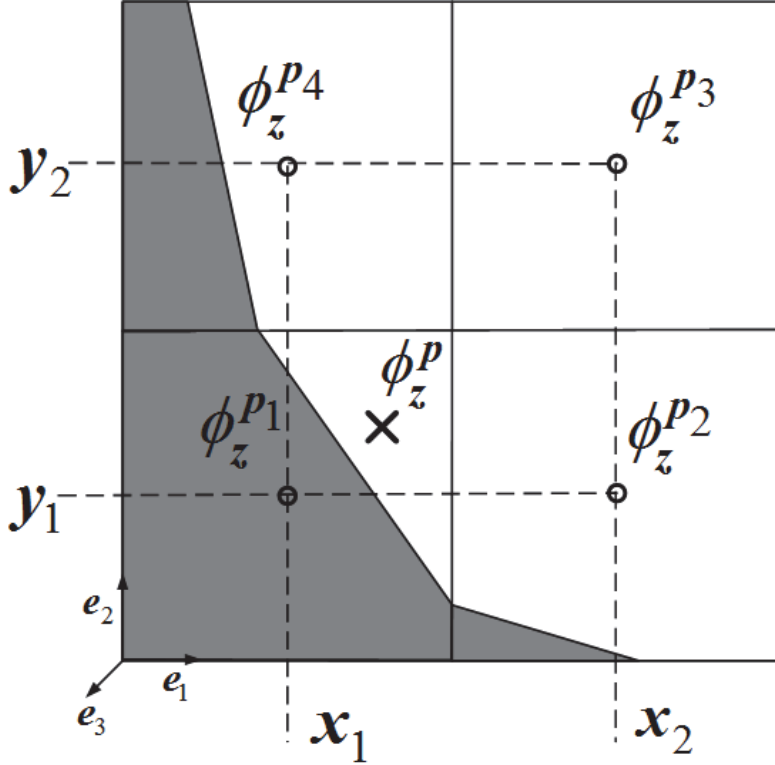
FIG. 1. *Stencil for the approximation of the normal derivative at the face centroid.*

3.3.1. Normal derivative approximation. In this case, we will follow the bi-linear interpolation method in [54]. First, centered differences in the normal direction are calculated at the centers of four faces including the face $A_{i \pm \frac{1}{2} e_s}$. Then iterated linear interpolations in the two axis directions parallel to $A_{i \pm \frac{1}{2} e_s}$ are performed to get an $O\left(h^2\right)$ accurate derivative value at the face centroid. It should be emphasized that by "face center" we refer to the center of the full rectangular face, which does not necessarily coincide with the face centroid $\boldsymbol{x}_{i \pm \frac{1}{2} e_s}$ calculated by quadrature rules.

As a concrete example, we consider the face $A_{\boldsymbol{i} + \frac{1}{2} e_3}$ with outward normal $\boldsymbol{e}_3$ as shown in Figure 1, where $\boldsymbol{p}_k$ $(k = 1 \dots 4)$ are the face centers and $\boldsymbol{p}$ is the face centroid. To simplify the formulas, we introduce the following notation:

$$(3.16) \qquad \phi^{\boldsymbol{i}}_{(l,m,n)} = \phi_{\boldsymbol{i} + l e_1 + m e_2 + n e_3}.$$

Then we define $\phi_z^{\boldsymbol{p}_k}$ as the centered difference in the direction of $\boldsymbol{e}_3$ at the face center $\boldsymbol{p}_k$, i.e.,

$$(3.17) \qquad \phi_z^{\boldsymbol{p}_1} = \frac{\phi^{\boldsymbol{i}}_{(0,0,1)} - \phi^{\boldsymbol{i}}_{(0,0,0)}}{h}, \; \phi_z^{\boldsymbol{p}_2} = \frac{\phi^{\boldsymbol{i}}_{(1,0,1)} - \phi^{\boldsymbol{i}}_{(1,0,0)}}{h},$$

$$(3.18) \qquad \phi_z^{\boldsymbol{p}_3} = \frac{\phi^{\boldsymbol{i}}_{(1,1,1)} - \phi^{\boldsymbol{i}}_{(1,1,0)}}{h}, \; \phi_z^{\boldsymbol{p}_4} = \frac{\phi^{\boldsymbol{i}}_{(0,1,1)} - \phi^{\boldsymbol{i}}_{(0,1,0)}}{h}.$$
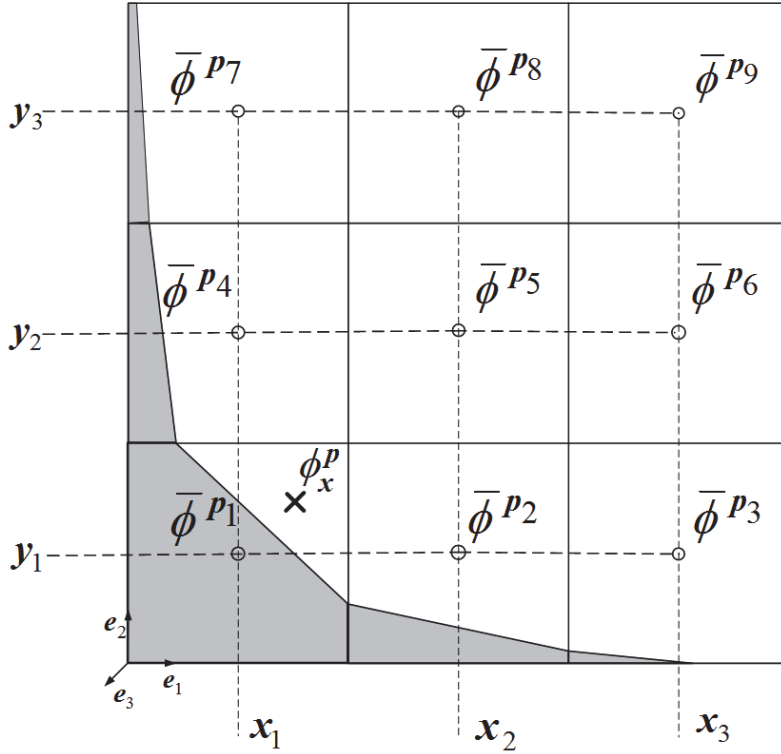
FIG. 2. *Stencil for the approximations of the parallel derivatives at the face centroid.*

Last, we perform the bilinear interpolation

$$(3.19) \qquad \phi_z^{\boldsymbol{p}} = \sum_{k=1}^{4} \lambda_z^k \phi_z^{\boldsymbol{p}_k},$$

where the interpolation coefficients are

$$(3.20) \qquad \lambda_z^1 = \frac{(x - x_2)(y - y_2)}{(x_1 - x_2)(y_1 - y_2)}, \ \lambda_z^2 = \frac{(x - x_1)(y - y_2)}{(x_2 - x_1)(y_1 - y_2)},$$

$$(3.21) \qquad \lambda_z^3 = \frac{(x - x_1)(y - y_1)}{(x_2 - x_1)(y_2 - y_1)}, \ \lambda_z^4 = \frac{(x - x_2)(y - y_1)}{(x_1 - x_2)(y_2 - y_1)}.$$

3.3.2. Parallel derivative approximation. In this case, we start by calculating centered averages in the normal direction at the centers of nine faces including face $A_{i \pm \frac{1}{2}e_s}$. Then we perform the biquadratic interpolation with the average values to get a quadratic polynomial in two variables. Finally, we calculate the partial derivatives of that polynomial at the face centroid $\boldsymbol{x}_{i \pm \frac{1}{2}e_s}$. Since the centered average is accurate to $O\left(h^2\right)$, and the biquadratic interpolation is accurate to $O\left(h^3\right)$, the aforementioned scheme results in parallel derivative approximations accurate to $O\left(h^2\right)$.

Similar to the situation in Figure 1, we consider the example of a face $A_{i + \frac{1}{2}e_3}$ with outward normal $\boldsymbol{e}_3$ as shown in Figure 2. As before, $\boldsymbol{p}_k$ $(k = 1 \ldots 9)$ and $\boldsymbol{p}$ are face centers and the face centroid, respectively. We fine $\overline{\phi}^{\boldsymbol{p}_k}$ as the centered average

at the face center $\boldsymbol{p}_k$, i.e.,

$$(3.22) \quad \bar{\phi}^{\boldsymbol{p}_1} = \frac{\phi^{\boldsymbol{i}}_{(0,0,1)} + \phi^{\boldsymbol{i}}_{(0,0,0)}}{2}, \ \bar{\phi}^{\boldsymbol{p}_2} = \frac{\phi^{\boldsymbol{i}}_{(1,0,1)} + \phi^{\boldsymbol{i}}_{(1,0,0)}}{2}, \ \bar{\phi}^{\boldsymbol{p}_3} = \frac{\phi^{\boldsymbol{i}}_{(2,0,1)} + \phi^{\boldsymbol{i}}_{(2,0,0)}}{2},$$

$$(3.23) \quad \bar{\phi}^{\boldsymbol{p}_4} = \frac{\phi^{\boldsymbol{i}}_{(0,1,1)} + \phi^{\boldsymbol{i}}_{(0,1,0)}}{2}, \ \bar{\phi}^{\boldsymbol{p}_5} = \frac{\phi^{\boldsymbol{i}}_{(1,1,1)} + \phi^{\boldsymbol{i}}_{(1,1,0)}}{2}, \ \bar{\phi}^{\boldsymbol{p}_6} = \frac{\phi^{\boldsymbol{i}}_{(2,1,1)} + \phi^{\boldsymbol{i}}_{(2,1,0)}}{2},$$

$$(3.24) \quad \bar{\phi}^{\boldsymbol{p}_7} = \frac{\phi^{\boldsymbol{i}}_{(0,2,1)} + \phi^{\boldsymbol{i}}_{(0,2,0)}}{2}, \ \bar{\phi}^{\boldsymbol{p}_8} = \frac{\phi^{\boldsymbol{i}}_{(1,2,1)} + \phi^{\boldsymbol{i}}_{(1,2,0)}}{2}, \ \bar{\phi}^{\boldsymbol{p}_9} = \frac{\phi^{\boldsymbol{i}}_{(2,2,1)} + \phi^{\boldsymbol{i}}_{(2,2,0)}}{2}.$$

Fitting the data $\bar{\phi}^{\boldsymbol{p}_k}$ ($k = 1 \dots 9$) with a biquadratic polynomial and calculating its x-directional derivatives at $\boldsymbol{p}$ leads to

$$(3.25) \qquad\qquad \phi^{\boldsymbol{p}}_x = \sum_{k=1}^{9} \lambda^k_x \phi^{\boldsymbol{p}_k}_x$$

with combination coefficients

$$(3.26) \qquad\qquad \lambda^1_x = \alpha_1 \beta_1, \ \lambda^2_x = \alpha_2 \beta_1, \ \lambda^3_x = \alpha_3 \beta_1,$$

$$(3.27) \qquad\qquad \lambda^4_x = \alpha_1 \beta_2, \ \lambda^5_x = \alpha_2 \beta_2, \ \lambda^6_x = \alpha_3 \beta_2,$$

$$(3.28) \qquad\qquad \lambda^7_x = \alpha_1 \beta_3, \ \lambda^8_x = \alpha_2 \beta_3, \ \lambda^9_x = \alpha_3 \beta_3,$$

where

$$\alpha_1 = \frac{(2x - x_2 - x_3)}{(x_1 - x_2)(x_1 - x_3)}, \ \alpha_2 = \frac{(2x - x_1 - x_3)}{(x_2 - x_1)(x_2 - x_3)}, \ \alpha_3 = \frac{(2x - x_1 - x_2)}{(x_3 - x_1)(x_3 - x_2)},$$

$$\beta_1 = \frac{(y - y_2)(y - y_3)}{(y_1 - y_2)(y_1 - y_3)}, \ \beta_2 = \frac{(y - y_1)(y - y_3)}{(y_2 - y_1)(y_2 - y_3)}, \ \beta_3 = \frac{(y - y_1)(y - y_2)}{(y_3 - y_1)(y_3 - y_2)}.$$

Similarly, we can construct interpolation $\phi^{\boldsymbol{p}}_y$. Both $\phi^{\boldsymbol{p}}_x$ and $\phi^{\boldsymbol{p}}_y$ are accurate to $O\left(h^2\right)$.

3.4. Boundary conditions. In this section, we discuss the differentiation of the Dirichlet boundary condition (3.11). Our method is a generalization of the approach proposed by Schwartz et al. [54]. As shown in Figure 3 we choose a nine-cell stencil on each of the two planes P_1 and P_2, both perpendicular to $\boldsymbol{e}_s$, where s is given by

$$(3.29) \qquad\qquad \left\{ s: \ \left| n^{\mathrm{B}}_s \right| \geq \left| n^{\mathrm{B}}_k \right|, \ k = 1, 2, 3 \right\}.$$

In other words, $\boldsymbol{e}_s$ is the axis direction closest to the boundary normal $\boldsymbol{n}^B$, $\boldsymbol{x}_B$ is the centroid of the partial boundary included in the cell, and $\boldsymbol{p}$ and $\boldsymbol{q}$ are the intersection points of $\boldsymbol{e}_s$ with planes P_1 and P_2, respectively. Then we define the distances from $\boldsymbol{x}_B$ to the intersection points: $d_1 = \|\boldsymbol{x}_{\mathrm{B}} - \boldsymbol{p}\|$ and $d_2 = \|\boldsymbol{x}_{\mathrm{B}} - \boldsymbol{q}\|$.

As mentioned before, we need to approximate the gradient $\nabla \phi_B = \left(\phi^{\mathrm{B}}_x, \phi^{\mathrm{B}}_y, \phi^{\mathrm{B}}_z, \right)$ at the partial boundary centroid $\boldsymbol{x}_{\mathrm{B}}$ to $O\left(h^2\right)$ accuracy. To simplify the following discussion, we assume $\boldsymbol{e}_s = \boldsymbol{e}_1$. Then the approximation of ϕ^{B}_x is different from those of ϕ^{B}_y and ϕ^{B}_z. For the calculation of ϕ^{B}_x, we first use biquadratic interpolation to calculate $\bar{\phi}^{\boldsymbol{p}}$ and $\bar{\phi}^{\boldsymbol{q}}$, which are $O\left(h^3\right)$ accurate approximations to $\psi(\boldsymbol{p})$ and $\psi(\boldsymbol{q})$. The value of $\bar{\phi}^{\boldsymbol{p}}$ is a linear combination of the nine cell-center values on plane P_1, and $\bar{\phi}^{\boldsymbol{q}}$ is calculated analogously with values on P_2. Then we combine the boundary
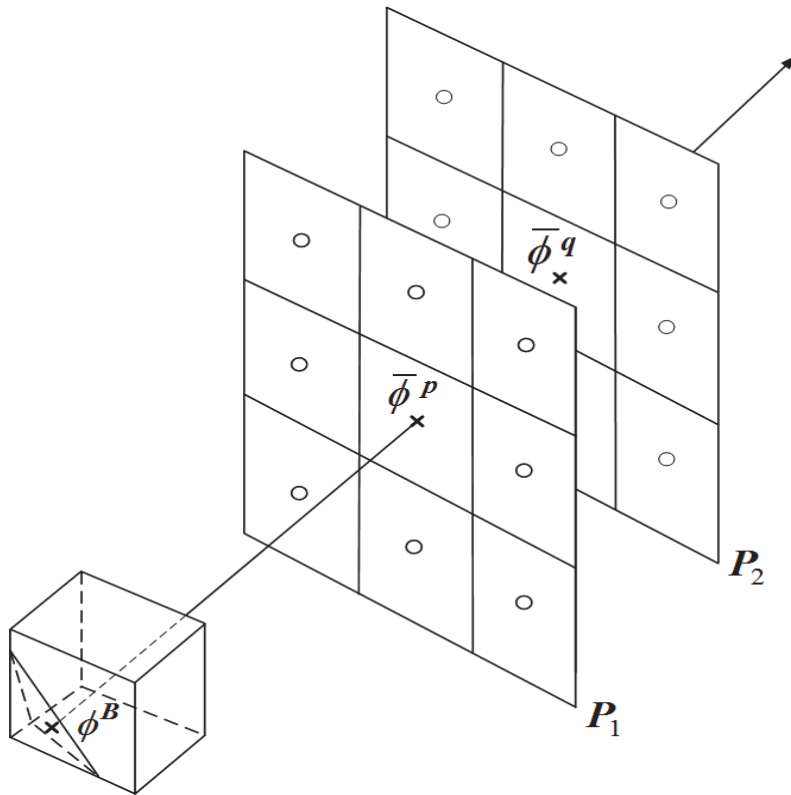
FIG. 3. *Stencil for the approximation of the derivatives at the boundary centroid.*

value ϕ^B determined by the Dirichlet condition with the intersection values $\bar{\phi}^p$ and $\bar{\phi}^q$ using the scheme given in [54] to construct

$$(3.30) \qquad \phi_x^B = \frac{1}{d_2 - d_1} \left(\frac{d_2}{d_1} \left(\phi^B - \bar{\phi}^p \right) - \frac{d_1}{d_2} \left(\phi^B - \bar{\phi}^q \right) \right).$$

To construct ϕ_y^B, we start by using the interpolation method in (3.25) to get $O\left(h^2\right)$ accurate approximations ϕ_y^p and ϕ_y^q with the nine cell-center values on P_1 and P_2, respectively. Then ϕ_y^B can be constructed by applying the following linear extrapolation to ϕ_y^p and ϕ_y^q:

$$(3.31) \qquad \phi_y^B = \frac{1}{d_2 - d_1} \left(d_2 \phi_y^p - d_1 \phi_y^q \right).$$

The same idea can be applied to the calculation of ϕ_z^B.

4. Verification. In this section, we verify the numerical algorithm with two tests. In the first test, we apply the EBM to solve the Poisson's equation with an anisotropic diffusion tensor in a 3D spherical domain. Second order convergence is observed by comparing numerical to analytical solutions. In the second test, we solve the voltage equation with both EBM and PF in a slab geometry, where nearly identical transmembrane potentials and conduction velocities of the depolarizing wave front are observed in regions away from the boundaries. All the test results confirm the accuracy and correctness of the EBM.

4.1. Poisson's equation in 3D spherical domain. Since the main challenge in solving the bidomain equations is the existence of elliptic operators with anisotropic diffusion tensors, we verify the new algorithm by solving an anisotropic Poisson equation. Within a spherical computational domain Ω with center $(0,0,0)$ and radius 0.5, we solve the Poisson's equation with the Dirichlet boundary condition as

$$(4.1) \qquad \nabla \cdot (D\phi(\mathbf{x})) = f(\mathbf{x}), \quad \mathbf{x} \in \Omega,$$

$$(4.2) \qquad \phi(\mathbf{x}) = \phi^B(\mathbf{x}), \quad \mathbf{x} \in \partial\Omega,$$

where the diffusion tensor D, the right-hand side function f, and the boundary value function ϕ^B are given as

$$(4.3) \qquad D = \frac{1}{3} \begin{bmatrix} 7 & 2 & 1 \\ 2 & 6 & -2 \\ 1 & -2 & 5 \end{bmatrix},$$

$$f(\mathbf{x}) = -\frac{76}{3}\sin(x)\sin(2y)\sin(3z) - 8\sin(x)\cos(2y)\cos(3z)$$

$$(4.4) \qquad + 2\cos(x)\sin(2y)\cos(3z) + \frac{8}{3}\cos(x)\cos(2y)\sin(3z),$$

$$(4.5) \qquad \phi^B(\mathbf{x}) = \sin(x)\sin(2y)\sin(3z).$$

The analytical solution to the above boundary value problem is

$$(4.6) \qquad \phi^e(\mathbf{x}) = \sin(x)\sin(2y)\sin(3z).$$

It is worth noting that the choice of this analytical solution is solely for the purpose of convergence order analysis and has no direct relation to the bidomain model. We use ϕ_i and ϕ_i^e to denote the numerical and corresponding exact solutions at the cell centroid x_i, and define the L_1, L_2, and L_∞ errors as

$$(4.7) \qquad \epsilon_1 = \sum_i |\phi_i - \phi_i^e| \, h^3 \kappa_i,$$

$$(4.8) \qquad \epsilon_2 = \left(\sum_i |\phi_i - \phi_i^e|^2 \, h^3 \kappa_i \right)^{\frac{1}{2}},$$

$$(4.9) \qquad \epsilon_\infty = \max_i |\phi_i - \phi_i^e|,$$

where h is the space step size and κ_i is the volume fraction. To estimate the order of convergence, we consider mesh sizes of 16, 32, 64, and 128, denoted by grids I, II, III, and IV, respectively. In Table 1, we show the orders of convergence deduced from the three types of errors under different mesh sizes. The entries from the last three columns of Table 1 confirm the second order accuracy of the method.

4.2. Comparison of EBM and PF. We compare EBM and PF for the solution of the voltage equation in a slab geometry. The transmembrane potential (V) and the conduction velocity (CV) of the depolarizing wave front are compared in the center of the slab, away from its boundaries. By this measure, the two methods are nearly identical. The reason for this near identity is that the compared statistics are

TABLE 1
Orders of convergence for three types of errors.

Error type	I	II	III	IV	I / II	II / III	III / IV
ϵ_1	6.13e-4	7.04e-5	1.47e-5	3.59e-6	3.12	2.26	2.03
ϵ_2	1.03e-3	9.52e-5	1.86e-5	4.64e-6	3.44	2.36	2.00
ϵ_∞	1.18e-2	1.20e-3	1.39e-4	1.87e-5	3.29	3.12	2.89

TABLE 2
CV error and convergence order comparison.

| Mesh size	PF error	PF order	EBB error	EBM order	PF − EBM
$15 \times 10 \times 25$	3.43e-02		3.51e-02		7.77e-02
$30 \times 20 \times 50$	1.89e-02	0.86	1.72e-02	1.03	1.71e-03
$60 \times 40 \times 100$	0.742e-02	1.35	0.612e-02	1.49	1.29e-03
$120 \times 80 \times 200$	0.151e-02	2.30	0.147e-02	2.06	3.14e-05
$240 \times 160 \times 400$					1.46e-06

not influenced by boundary effects, while it is only in the boundary effects that the methods differ.

We choose the slab region $[0, 1.0] \times [0, 0.5] \times [0, 2.0]$ (cm). The direction of cardiac fibers is chosen to be parallel to the z-axis. An initial stimulus is applied in a region at the bottom of the slab.

Five mesh sizes are considered, starting from $\Delta x = 1.0$ mm, with each following mesh refined by a factor of 2. The starting Δx is quite coarse compared to the typical size of cardiac cells, which is approximately $100\,\mu$m long and 10–$25\,\mu$m in diameter [55]. The finest mesh is used to calculate errors in the other four cases. The difference for this fiducial grid is smaller than the mesh differences, indicating that the two codes are converging to a common solution.

Table 2 shows the errors and order of convergence for CV. In Table 3 we present the error analysis and convergence orders based on comparison of L_1 norms of V. It is shown that both PF and EBM methods converge in first order. To achieve second order accuracy in both time and space, second order operator splitting schemes, e.g., Strang splitting [56], need to be applied to the bidomain equations.

5. Applications. The main motivation of this work is to develop an improved numerical method to support the study of the low-energy antifibrillation pacing initiative [40], whose effect depends on the successful generation of virtual electrodes in the vicinities of heterogeneities in the myocardium. As a result, the accurate resolution of small features, e.g., blood vessels, plays an essential role in defibrillation simulations. In this section, we first demonstrate the strength of our EBM method by showing the voltage distribution on blood vessel walls during a defibrillation event. The calculation is representative of ones needed to determine the smallest relevant blood vessels for consideration. With the blood vessel size fixed, a systematic statistical analysis gives suggestions on the choice of appropriate mesh resolutions for practical defibrillation simulations on complex 3D domains. Because optimization, V&V, and UQ typically require a large number of simulations, determination of minimum mesh requirements is important.

5.1. Defibrillation simulation. Defibrillation consists of one or more strong voltage pulses applied across the heart. This voltage is originally applied to the extracellular space, and so the coupling of this signal to the intracellular voltages

TABLE 3
$V(L_1\text{-}norm)$ error and convergence order comparison.

Mesh size	PF error	PF order	EBM error	EBM order	PF − EBM
$15 \times 10 \times 25$	5.19e-01		5.30e-01		7.44e-02
$30 \times 20 \times 50$	2.06e-01	1.34	1.86e-01	1.51	2.11e-02
$60 \times 40 \times 100$	0.729e-01	1.50	0.689e-01	1.43	4.09e-03
$120 \times 80 \times 200$	0.178e-01	2.03	0.174e-01	1.99	5.11e-04
$240 \times 160 \times 400$					1.08e-04
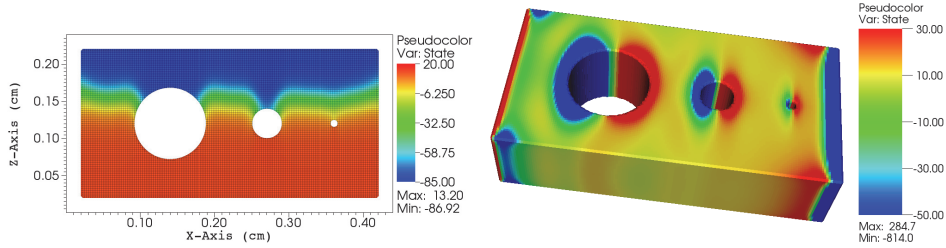
FIG. 4. *Transmembrane potential (mV) in a slab before (left) and after (right) applying the defibrillation shock.*

is essential for defibrillation to succeed. The dual voltage systems and the coupling between them is described by the bidomain model as discussed in section 2.

Our simulation domain is chosen to be a slab taken from a segment of the heart wall, with dimensions $[0, 4] \times [0, 1] \times [0, 2]$ (mm). The spatial resolution is 0.025 (mm) and the time step size is 0.01 (ms). The values of conductivities of the cardiac tissue $\mathbb{H}$ and the surrounding tissue $\mathbb{T}$ are chosen as in [53]. As shown in Figure 4, three blood vessels are placed perpendicular to the xz-plane, with radii ranging from 50 to 500 microns, which are typical sizes found in coronary vasculature [40, 4]. It should be emphasized that although the two larger vessels, 40 and 16 mesh cells in diameter, respectively, can be resolved in both PF and EBM methods, the smallest one with only 4 mesh cells in diameter cannot be captured correctly in the PF model, due to its artificial transition layers.

As shown in the left part of Figure 4, an initial stimulus is applied to the bottom of the slab, resulting a depolarization wave front propagating upwards. When the wave front passes the blood vessels, a defibrillation shock of strength $5\,\mathrm{V/cm}$ in the x-direction is applied to the slab. Shortly after the defibrillation shock, as illustrated in the right part of Figure 4, voltage drops are observed across all three blood vessels. In fact, the electrical discontinuity introduced by the blood vessels acts as a source for the transfer of the shock energy from the intracellular domain to the cardiac cell domain, which expedites the defibrillation process.

5.2. Mesh resolution. The determination of a proper mesh resolution is a prerequisite for any defibrillation simulation. To make suggestions for the choice of appropriate mesh resolutions for practical simulations on complex domains, a systematic statistical analysis is performed using a simplified slab geometry as that in section 5.1. We consider a slab region $[-0.2, 0.2] \times [-0.2, 0.2] \times [-0.2, 0.2]$ (mm), in which a blood vessel with diameter 0.1 mm is located perpendicular to the xz-plane. The cardiac cells in the slab are initialized by the resting membrane potential, and then a shock of strength 5V/cm in the x-direction is applied for 0.1 ms.

To perform a statistical analysis of the effect of the mesh resolution on wave propagation across the blood vessel, we perform multiple simulations with different combinations of mesh resolutions and positions of the blood vessel. Eight resolution levels are adopted, with the diameter of the blood vessel ranging from $2\Delta x$ to $8\Delta x$ in mesh units. For each mesh resolution, we choose one of 25 positions within the small region $[-\Delta x,\ \Delta x]\times[-\Delta x,\ \Delta x]$ as the crossing point of the blood vessel axis and the xz-plane. The voltage drops across the blood vessel are calculated for different combinations, and the results are summarized in Figure 5.

In Figure 5, the bottom and the top of the box are the first quartile (Q_1) and the third quartile (Q_3), respectively. The band inside the box denotes the median. The lower and upper ends of the whisker are the minimum and maximum of the data. From the plot, we can observe a fast convergence of the voltage drop as the resolution increases. With only a $4\Delta x$ diameter, the relative error in the voltage drop calculation is already within 10%, when taking the $8\Delta x$ values as accurate. Moreover, even in the case of a resolution as low as $2\Delta x$, the calculated voltage drops are still within a reasonably small neighborhood of the $8\Delta x$ resolution results. In conclusion, four or fewer cells across the blood vessel should suffice in a whole heart simulation for the purpose of UQ analysis, while higher resolutions are necessary for fully accurate whole heart simulations. Further efforts to improve the algorithm could reduce these numbers.

6. Conclusions. We extend the finite volume EBM, originally proposed by Johansen and Colella [32], to the solutions of elliptic and parabolic equations involving anisotropic diffusion tensors and indicate a methodology for construction of solutions of an arbitrary order of accuracy. A new type of sharp boundary electrocardiac simulation tool based on the EBM method is introduced and applied to defibrillation studies using the bidomain model. It is shown that the new method is second order accurate uniformly up to boundaries, which particularly aids the resolution of small
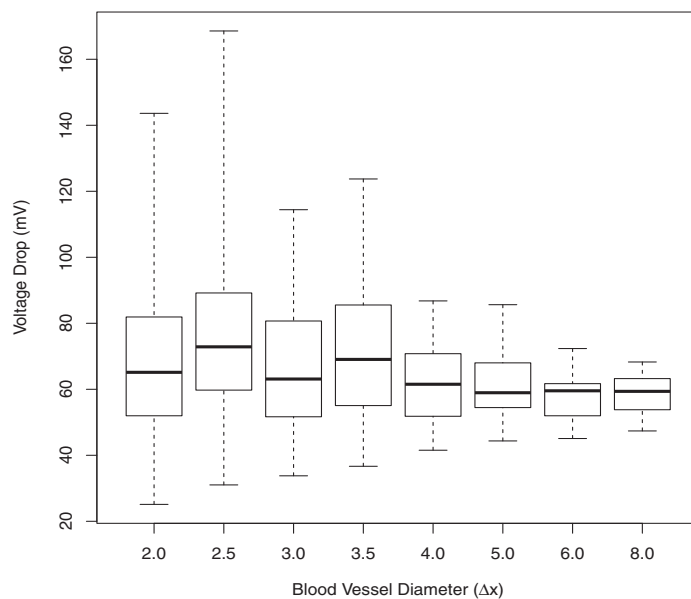

FIG. 5. *Variation of the voltage drop across the blood vessel under mesh refinement.*

features in the heart tissue. This capability lends our method to the promising field of low-energy defibrillation, where the generation of virtual electrodes around small heterogeneities in the myocardium plays an indispensable role. To improve the efficiency as well as to keep the accuracy of practical simulations, a systematic statistical analysis is performed in order to determine the appropriate mesh resolution. It is shown that four mesh cells are needed to resolve the finest blood vessels for the purpose of UQ analysis. However, for highly accurate whole heart simulations, the usage of more mesh cells is recommended. To further improve the accuracy, in the future, we plan to add more physiological details, such as the 3D complex heart geometry, realistic myocardial fiber orientations, and more complete models of ionic currents, into our model. Extensions to higher order accuracy may be beneficial to further reduce resolution requirements. Second order accuracy in time (not considered here) will require Strang splitting of the sequential equation solution method.

REFERENCES

[1] H. Arevalo, B. Rodriguez, and N. A. Trayanova, *Arrhythmogenesis in the heart: Multiscale modeling of the effects of defibrillation shocks and the role of electrophysiological heterogeneity*, Chaos, 17 (2007), 015103.

[2] T. Ashihara and N. A. Trayanova, *Cell and tissue responses to electric shocks*, Europace, 7 (2005).

[3] T. Ashihara and N. A. Trayanova, *Tunnel propagation of postshock activations as a hypothesis for fibrillation induction and isoelectric window*, Circulation Research, 102 (2008).

[4] M. J. Bishop, G. Plank, and E. Vigmond, *Investigating the role of coronary vascluture in the mechanisms of defibrillation*, Circulation Arrthymia Electrophysiology, 5 (2012), pp. 210–219.

[5] V. E. Bondarenko, G. C. L. Bett, and R. L. Rasmusson, *A model of graded calcium release and L-type Ca2+ channel inactivation in cardiac muscle*, Amer. J. Physiology Heart Circulatory Physiology, 286 (2004), pp. 1154–1169.

[6] A. Bueno-Orovio, V. M. Perez-Garcia, and F. H. Fenton, *Spectral methods for partial differential equations in irregular domains: The spectral smoothed boundary method*, SIAM J. Sci. Comput, 28 (2006), pp. 886–900.

[7] G. T. Buzzard, J. J. Fox, and F. Siso-Nadal, *Sharp interface and voltage conservation in the phase field method: Application to cardiac electrophysiology*, SIAM J. Sci. Comput., 34 (2008), pp. 837–854.

[8] M. Chebbok, A. Squires, J. Schroeder-Schetelig, M. Zabel, G. Hasenfuss, E. Bodenschatz, F. Fenton, and S. Luther, *Low-energy anti-fibrillation pacing (LEAP): A gentle, non traumatic defibrillation option*, European Heart Journal, 33 (2012), pp. 381–381.

[9] E. M. Cherry and F. H. Fenton, *A tale of two dogs: Analyzing two models of canine ventricular electrophysiology*, Amer. J. Physiology Heart Circulatory Physiology, 292 (2007), pp. 43–55.

[10] E. M. Cherry and F. H. Fenton, *Effects of boundaries and geometry on the spatial distribution of action potential duration in cardiac tissue*, J. Theoret. Biol., 285 (2011), pp. 164–176.

[11] E. M. Cherry, F. H. Fenton, and R. F. Gilmour, *Mechanisms of ventricular arrhythmias: A dynamical systems-based perspective*, Amer. J. Physiology Heart Circulatory Physiology, 302 (2012), pp. 2451–2463.

[12] G. Chevant and J. Jaffre, *Mathematical Models and Finite Elements for Reservoir Simulation*, North-Holland, New York, 1987.

[13] R. Clayton and A. Panfilov, *A guide to modelling cardiac electrical activity in anatomically detailed ventricles*, Progr. Biophys. Molecular Biol., 96 (2008), pp. 19–43.

[14] R. H. Clayton, O. Bernus, E. M. Cherry, H. Dierckx, F. H. Fenton, L. Mirabella, A. V. Panfilov, F. B. Sachse, G. Seemann, and H. Zhang, *Models of cardiac tissue electrophysiology: Progress, challenges and open questions*, Progr. Biophys. Molecular Biol., 104 (2011), pp. 22–48.

[15] P. Colella, M. Dorr, J. Hittinger, D. Martin, and P. McCorquodale, *High-order finite-volume adaptive methods on locally rectangular grids*, J. Phys. Conf. Ser., 180 (2009), pp. 12010–12010.

[16] P. Colli-Franzone, L. F. Pavarino, and S. Scacchi, *Exploring anodal and cathodal make and break cardiac excitation mechanisms in a 3D anisotropic bidomain model*, Math. Biosci., 230 (2011), pp. 96–114.

[17] R. K. Crockett, P. Colella, and D. T. Graves, *A Cartesian grid embedded boundary method for solving the poisson and heat equations with discontinuous coefficients in three dimensions*, J. Comput. Phys., 230 (2010), pp. 2451–2469.

[18] A. Dadone and B. Grossman, *Ghost-cell method for inviscid two-dimensional flows on cartesian grids*, AIAA J., 42 (2004), pp. 2499–2507.

[19] G. Duckett and D. Barkley, *Modeling the dynamics of cardiac action potential*, Phys. Rev. Lett., 85 (2000), pp. 884–884.

[20] I. R. Efimov, R. A. Gray, and B. J. Roth, *Virtual electrodes and deexcitation: New insights into fibrillation induction and defibrillation*, J. Cardiovascular Electrophysiology, 11 (2000), pp. 339–353.

[21] I. R. Efimov, M. Kroll, and P. J. Tchou, *Cardiac Bioelectric Therapy: Mechanisms and Practical Implications*, Springer Science & Business Media, New York, 2008.

[22] F. Fenton and E. Cherry, *Models of cardiac cell*, Scholarpedia, 3 (2008), pp. 1868–1868.

[23] F. Fenton, E. Cherry, A. Karma, and W. Rappel, *Modeling wave propagation in realistic heart geometries using the phase-field method*, Chaos, 15 (2005), pp. 13502–13502.

[24] F. Fenton and A. Karma, *Vortex dynamics in three-dimensional continuous myocardium with fiber rotation: Filament instability and fibrillation*, Chaos, 8 (1998), pp. 20–47.

[25] F. H. Fenton, A. Gizzi, C. Cherubini, N. Pomella, and S. Filippi, *Role of temperature on nonlinear cardiac dynamics*, Phys. Rev. E, 87 (2013), 042717.

[26] F. H. Fenton, S. Luther, E. M. Cherry, N. F. Otani, V. Krinsky, A. Pumir, E. Bodenschatz, and R. F. Gilmour, *Termination of atrial fibrillation using pulsed low-energy far-field stimulation*, Circulation, 120 (2009), pp. 467–476.

[27] S. Filippi, A. Gizzi, C. Cherubini, S. Luther, and F. H. Fenton, *Mechanistic insights into hypothermic ventricular fibrillation: The role of temperature and tissue size*, Europace, 16 (2014), pp. 424–434.

[28] S. N. Flaim, W. R. Giles, and A. D. McCulloch, *Contributions of sustained INa and IKv43 to transmural heterogeneity of early repolarization and arrhythmogenesis in canine left ventricular myocytes*, Amer. J. Physiology Heart Circulatory Physiology, 291 (2006), pp. 2617–2629.

[29] Centers for Disease Control and Prevention, *State-specific mortality from sudden cardiac death–United States*, 1999, MMWR Morbidity Mortality Weekly Report, 51 (2002), pp. 123–123.

[30] F. Gibou, R. Fedkiw, L.-T. Cheng, and M. Kang, *A second-order-accurate symmetric discretization of the poisson equation on irregular domains*, J. Comput. Phy., 176 (2002), pp. 205–227.

[31] J. Glimm, J. W. Grove, X.-L. Li, and N. Zhao, *Simple front tracking*, in Nonlinear Partial Differential Equation, Contemp. Math. 238, G.-Q. Chen and E. DiBenedetto, eds., AMS, Providence, RI, 1999, pp. 133–149.

[32] H. Johansen and P. Colella, *A Cartesian grid embedded boundary method for Poisson's equation on irregular domains*, J. Comput. Phys., 147 (1998), pp. 60–85.

[33] J. P. Wikswo, Jr., and B. J. Roth, *Virtual electrode theory of pacing*, in Cardiac Bioelectric Therapy, Springer, New York, 2009, pp. 283–330.

[34] A. Karma, *Electrical alternans and spiral wave breakup in cardiac tissue*, Chaos, 4 (1994), pp. 461–472.

[35] W. Krassowska and J. Neu, *Effective boundary conditions for syncytial tissues*, IEEE Trans. Biomed. Engrg., 41 (1994), pp. 143–150.

[36] S. S. Lee and R. A. Westmann, *Application of high-order quadrature rules to time-domain boundary element analysis of viscoelasticity*, Int. J. Numer. Methods Eng., 38 (1995), pp. 607–629.

[37] Z. Li, *An overview of the immersed interface method and its applications*, Taiwanese J. Math., 7 (2003), pp. 1–49.

[38] C. M. Lloyd, J. R. Lawson, P. J. Hunter, and P. F. Nielsen, *The CellML model repository*, Bioinformatics, 24 (2008), pp. 2122–2123.

[39] R. Lohner and J. D. Baum, *Adaptive h-refinement on 3D unstructured grids for transient problems*, Internat. J. Numer. Methods Fluids, 14 (1992), pp. 1407–1419.

[40] S. Luther, F. H. Fenton, B. G. Kornreich, A. Squires, P. Bittihn, D. Hornung, M. Zabel, et al., *Low-energy control of electrical turbulence in the heart*, Nature, 475 (2011), pp. 235–239.

[41] P. McCorquodale, P. Colella, and H. Johansen, *A Cartesian grid embedded boundary method for the heat equation on irregular domains*, J. Comput. Phys., 273 (2001), pp. 620–635.

[42] C. C. Mitchell and D. G. Schaeffer, *A two-current model for the dynamics of cardiac membrane*, Bull. Math. Biol., 65 (2003), pp. 767–793.

[43] R. Mittal and G. Iaccarino, *Immersed boundary methods*, Annu. Rev. Fluid Mech., 37 (2005), pp. 239–261.

[44] K. H. Tusscherand A. V. Panfilov, *Modelling of the ventricular conduction system*, Progr. Biophys. Molecular Biol., 96 (2008), pp. 152–170.

[45] P. Pathmanathan, M. S. Shotwell, D. J. Gavaghan, J. M. Cordeiro, and R. A. Gray, *Uncertainty quantification of fast sodium current steady-state inactivation for multi-scale models of cardiac electrophysiology*, Progr. Biophys. Molecular Biol., 117 (2015), pp. 4–18.

[46] C. S. Peskin, *Numerical analysis of blood-flow in heart*, J. Comput. Phys., 25 (1977), pp. 220–252.

[47] B. Phibbs, *The Human Heart: A Basic Guide to Heart Disease*, Lippincott Williams & Wilkins, Philadelphia, 2007.

[48] J. M. Rogers and A. D. McCulloch, *A collocation-Galerkin finite element model of cardiac action potential propagation*, IEEE Trans. Biomed. Engrg., 41 (1994), pp. 743–757.

[49] J. M. Rogers and A. D. McCulloch, *Wave front fragmentation due to ventricular geometry in a model of the rabbit heart*, Chaos, 12 (2002), pp. 779–787.

[50] B. J. Roth, *Nonsustained reentry following successive stimulation of cardiac tissue through a unipolar electrode*, J. Cardiovascular Electrophysiology, 8 (1997), pp. 768–778.

[51] A. Sambelashvili, V. P. Nikolsky, and I. R. Efimov, *Virtual electrode theory explains pacing threshold increase caused by cardiac tissue damage*, Amer. J. Physiology Heart Circulatory Physiology, 286 (2004), pp. 2183–2194.

[52] R. Samulyak, J. Du, J. Glimm, and Z. Xu, *A numerical algorithm for MHD of free surface flows at low magnetic Reynolds numbers*, J. Comput. Phys., 226 (2007), pp. 1532–1546.

[53] R. W. Dos Santos, G. Plank, S. Bauer, and E. J. Vigmond, *Preconditioning techniques for the bidomain equations*, in Domain Decomposition Methods in Science and Engineering, Springer, Berlin, 2005, pp. 571–580.

[54] P. Schwartz, M. Barad, P. Colella, and T. Ligocki, *A Cartesian grid embedded boundary method for the heat equation and poisson's equation in three dimensions*, J. Comput. Phys., 211 (2006), pp. 531–550.

[55] D. Sevcovic, *The cardiac muscle cell*, Bioessays, 22 (2000), pp. 188–199.

[56] G. Strang, *On the construction and comparison of difference schemes*, SIAM J. Numer. Anal., 5 (1968), pp. 506–517.

[57] G. Strang and G. Fix, *An Analysis of the Finite Element Method*, Prentice-Hall, Englewood Cliffs, N.J., 1973.

[58] L. Tang and J. D. Baeder, *Uniformly accurate finite difference schemes for p-refinement*, SIAM J. Sci. Comput., 20 (1998), pp. 1115–1131.

[59] L. Tung, *A Bi-domain Model for Describing Ischemic Myocardial D-C Potentials*, Ph.D. thesis, MIT, 1978.

[60] S. Wang, J. Glimm, R. Samulyak, X. Jiao, and C. Diao, *An Embedded Boundary Method for Two Phase Incompressible Flow*, arXiv:1304.5514, 2013.

[61] S. Wang, R. V. Samulyak, and T. Guo, *An embedded boundary method for elliptic and parabolic problems with interfaces and application to multi-material systems with phase transitions*, Acta Math. Sci., 30B (2010), pp. 499–521.

[62] M. A. Watanabe, F. H. Fenton, S. J. Evans, H. M. Hastings, and A. Karma, *Mechanisms for discordant alternans*, Comput. Fluids, 12 (2001), pp. 196–206.

[63] J. B. White, G. P. Walcott, A. E. Pollard, and R. E. Ideker, *Myocardial discontinuities: A substrate for producing virtual electrodes that directly excite the myocardium by shocks*, Circulation, 97 (1998), pp. 1738–1745.

[64] L. Ying, G. Biros, and D. Zorin, *A high-order 3D boundary integral equation solver for elliptic PDEs in smooth domains*, J. Computat. Phys., 219 (2006), pp. 247–275.